

Article

Porous Mullite Ceramic Modification with Nano-WO₃

Ludmila Mahnicka-Goremikina ^{1,*}, Ruta Svinka ¹, Visvaldis Svinka ¹, Vadims Goremikins ², Svetlana Ilic ³ , Liga Grase ¹ , Inna Juhneva ¹, Maris Rundans ¹, Toms Valdemars Eiduks ¹  and Arturs Pludons ¹

¹ Institute of Materials and Surface Engineering, Faculty of Materials Science and Applied Chemistry, Riga Technical University, Paula Valdena st. 3/7, LV-1048 Riga, Latvia; ruta.svinka@rtu.lv (R.S.); visvaldis.svinka@rtu.lv (V.S.); liga.grase@rtu.lv (L.G.); inna.juhneva@rtu.lv (I.J.); maris.rundans@rtu.lv (M.R.); toms-valdemars.eiduks@rtu.lv (T.V.E.); arturs.pludons@rtu.lv (A.P.)

² Institute of Structural Engineering and Reconstruction, Riga Technical University, Kipsalas st. 6A, LV-1048 Riga, Latvia; vadims.goremikins@rtu.lv

³ Department of Materials, Vinča Institute of Nuclear Sciences—National Institute of Republic of Serbia, University of Belgrade, Mike Petrovića Alasa 12-14, P.O. Box 522, 11001 Belgrade, Serbia; svetlanailic@vin.bg.ac.rs

* Correspondence: mahnicka@inbox.lv

Abstract: Mullite and mullite–alumina ceramics materials with dominance of the mullite phase are used in different areas of technology and materials science. Porous mullite ceramics materials can be used simultaneously as refractory heat insulators and also as materials for constructional elements. The purpose of this work was to investigate the WO₃ nanoparticle influence on the evolution of the aluminum tungstate and zircon crystalline phases in mullite ceramics due to stabilization effects caused by different microsize ZrO₂ and WO₃. The use of nano-WO₃ prevented the dissociation of zircon in the ceramic samples with magnesia-stabilized zirconia (MSZ), increased porosity by approximately 60 ± 1%, increased the intensity of the aluminum tungstate phase, decreased bulk density by approximately 1.32 ± 0.01 g/cm³, and increased thermal shock resistance by ensuring a loss of less than 5% of the elastic modulus after 10 cycles of thermal shock.

Keywords: mullite; aluminum tungstate; zircon; porous ceramic; tungsten oxide; zirconia



Citation: Mahnicka-Goremikina, L.; Svinka, R.; Svinka, V.; Goremikins, V.; Ilic, S.; Grase, L.; Juhneva, I.; Rundans, M.; Eiduks, T.V.; Pludons, A. Porous Mullite Ceramic Modification with Nano-WO₃. *Materials* **2023**, *16*, 4631. <https://doi.org/10.3390/ma16134631>

Academic Editor: Ales Buyakov

Received: 23 May 2023

Revised: 13 June 2023

Accepted: 14 June 2023

Published: 27 June 2023



Copyright: © 2023 by the authors. Licensee MDPI, Basel, Switzerland. This article is an open access article distributed under the terms and conditions of the Creative Commons Attribution (CC BY) license (<https://creativecommons.org/licenses/by/4.0/>).

1. Introduction

The relevance of new investigations in mullite ceramic synthesis and modification, as well as of new areas of mullite ceramics application, has been going on for 10 years. The popularity of research on mullite ceramics has increased significantly over the past 4 years (from 2019 to 2022); the increased number of published research articles confirms that. Moreover, mullite ceramics are actively being studied as high-temperature filters and thermal insulation materials [1,2]. Such thermal insulation mullite ceramic can be used to prevent heat losses and heat release to the environment, as well as to avoid damage caused by contact with high-temperature objects [2–7].

Improving the thermal insulation properties and thermal stability of mullite ceramics can be observed by increasing such material's porosity, modifying by the addition of mullite whiskers [8,9] or by in situ formed mullite whiskers [10,11], or with nanosized oxides [12–14]. The pores' morphology and size have important significance for refractory castables' thermal properties. Ceramic structure, crystal morphology, and pore size can be changed by ceramic modification with nanoparticles [12,15]. The high specific surface area of nanometer size components increases the reactivity of particles and, as a result, the temperature required to start the sintering process will be decreased. The addition of nanosized oxides to refractory ceramics has an impact on the material's properties. Research work has adopted nanosized TiO₂, ZrO₂, and MgO as sintering additives for technical ceramic modification [16]. Therefore, previous work has shown that nano-TiO₂ could enhance the

mechanical properties, for example, of high-alumina castables [17], yttria-stabilized zirconia (3YSZ) ceramics [18], and zirconia/alumina ceramics [19]. Esmaili et al. [20] reported that the addition of nano-TiO₂ promotes mullitization, increases sintering, and improves the mechanical properties of porcelains. In the case of MgO–CaO refractory ceramic, the addition of nano-ZrO₂ improves densification and resistance to hydration [21]. Gogtas et al. reported that nano-yttria-stabilized zirconia and nano-ZrO₂ particles [22] improve the toughness of Al₂O₃-based matrices. There is growing interest in the use of oxides, such as WO₃, to change the properties of technical ceramic. Due to such properties as catalytic activity [23], the existence of amorphous, mesosized, and nanosized porous structures, abundant quantity on earth, and nontoxic nature, WO₃ has found wide application in the different fields of technical ceramics. Micro- and nanosize powder WO₃ can be applied as ceramics for functional materials, capacitors, and varistors; special ceramic membranes for photocatalytic processes; ceramics for gas detection; special ceramic films; and thermoelectric ceramics for high-temperature applications [24–27]. Paul et al. investigated highly dispersed silver nanoparticles on tungsten oxide nanorods for photoelectrocatalytic CO₂ reduction under visible light irradiation [28] and as effective catalysts of benzyl alcohol dehydrogenation [29]. The influence of WO₃ on refractory porous mullite ceramic has been little studied. Our previous investigations confirmed that micro-WO₃ application as a mullite doping additive accelerates the process of mullitization, which allows for decreasing the sintering temperature of mullite ceramic [30]. The scientific interest in research is caused by the lack of detailed studies on the influence of nano-WO₃ on mullite ceramics' functional properties.

The novelty of this study lies in the use of nano-WO₃ in combination with micro-ZrO₂ and micro-WO₃ and the investigation of the mullitization improvement in porous mullite ceramic. An increase in thermal shock resistance and the formation of phases with a low or negative coefficient of linear thermal expansion allow for the use of such ceramics both at elevated and sharply changing temperatures.

2. Raw Materials and Testing Methods

2.1. Raw Materials

Two different Nabalox aluminas— α -Al₂O₃ with an average particle size of 2 μ m and γ -Al₂O₃ with $d_{50} = 80$ μ m were purchased from Nabaltec AG of Germany. MEKA kaolin ($d_{50} = 1.5$ μ m; SiO₂—56.5 wt%, Al₂O₃—31.0 wt%) was supplied by the German company Amberger Kaolinwerke. Zirconia stabilized with 2.8 mol% of magnesia with an average particle size of 0.8 μ m was purchased from Goodfellow, United Kingdom. Zirconia stabilized with 8 mol% of yttria with $d_{50} = 0.5$ μ m, SiO₂ amorphous with $d_{50} = 3$ –5 μ m, micro-WO₃ with $d_{50} = 5$ μ m, and nano-WO₃ with $d_{50} = 50$ nm were supplied by GetNano-Materials, France. Aluminum paste Aquapor-9008 with $70 \pm 2\%$ content of solid part and with $d_{50} = 12$ μ m was acquired from German Schlenk Metallic Pigments GmbH. It is well known that a reduction in the raw component particle size promotes the sintering of ceramics due to increased contacting particle surface area. The purpose of choosing micro- and nanosized WO₃ was to study the potential influence of the reduction in particle size, from micro- to nanosize, on the properties of the obtained ceramics.

2.2. Material Proportions

The base of the all mullite ceramics samples was prepared from 2 types of aluminas: alpha and gamma, kaolin, and amorphous SiO₂. In order to meet mullite stoichiometry, Al₂O₃ and SiO₂ were set at a 2.57:1 ratio. The total amount of Al₂O₃ consisted of $\frac{3}{4}$ γ -Al₂O₃ and $\frac{1}{4}$ α -Al₂O₃. Kaolin was used at 30 wt%. Different microsized ZrO₂ sources, such as yttria-stabilized zirconia (8 mol% Y₂O₃—YSZ) and magnesia-stabilized zirconia (2.8 mol% MgO—MSZ), were used in a mixture with microsized WO₃ for ceramic modifications. The ratios of the different stabilized microsized zirconia and microsized tungsten oxide were 1:1 and 1:2 of wt%. Nanosized WO₃ was used at 1 wt% in all compositions. The A1 and A2 samples were the compositions with microsized yttria-stabilized zirconia and tungsten

trioxide, respectively, in a 1:1 ratio plus nano-WO₃ and 1:2 plus nano-WO₃. The A3 and A4 samples were the compositions with microsized MSZ and microsized WO₃, respectively, in a 1:1 ratio plus nano-WO₃ and 1:2 plus nano-WO₃.

2.3. Sample Preparation Method

Ceramics samples were prepared by slip casting of the concentrated raw materials slurry. The distilled water percentage was approximately 40 ± 2 wt%. A suspension of aluminum paste with water was added into the raw materials slurry for pore forming purposes and then mixed for approximately 10 min. Kaolin as a binder and uniform mixing using a laboratory mixer allows for obtaining a uniform distribution of all components in the final slurry and prevents sedimentation of particles. The prepared raw material slurries were slip casted into molds. The pores of the investigated mullite ceramics were obtained due to the H₂ evolution that was formed due to the reaction between the Al paste and H₂O. The samples were solidified at room temperature and dried at 100 °C for 24 h. The samples were synthesized at 1600 °C with a heating rate of 4.2 °C/min and with holding at T_{max} for 1 h. The fired samples' cooling rate was the same as the rate of heating. The chosen heating rate was "industry average"—it was specifically chosen as a compromise between a slow heating rate and thus increased production costs and a fast heating rate, which, although being economically favorable, may be detrimental to product quality.

2.4. X-ray Diffraction Analysis

The crystalline phases of the sintered ceramics materials were analyzed using X-ray diffraction equipment BRUKER D8 Advance with a sealed ceramic copper X-ray tube, 40 kV voltage on copper anode, 40 mA of current intensity, detector 0d Sol-x, 0.1 mm of receiving slit, 0.6 mm of divergence slit, range of the measurement angle 10–80 2θ°, step scan mode, step size 0.008 2θ°, and time per step 6 s.

2.5. Scanning Electron Microscopy

The microstructures of the sintered samples were investigated using two scanning electron microscopes. The first was a Hitachi TM3000—TableTop SEM from Tokyo, Japan with an electron beam energy of 5 keV and 15 keV. The second high-resolution SEM was an FEI Nova NanoSEM 650 (Eindhoven, The Netherlands) with an electron beam energy of 10 keV. The low vacuum mode was used for microstructure observation; therefore, metal sputtering was not used. Energy dispersive mapping analysis was performed for certain samples.

2.6. Apparent Porosity

Archimedes' principle and mathematical calculations were used for apparent porosity determination after soaking the samples in distilled water, respectively, based on European standard EN 623-2 [31]. The value of the apparent porosity P was calculated by Equation (1), and the value of water uptake W was calculated by Equation (2):

$$P = ((m_3 - m_1)/(m_3 - m_2)) \times 100, \quad (1)$$

$$W = ((m_3 - m_1)/m_1) \times 100, \quad (2)$$

where m_1 is the mass of the sample in the dry state, m_2 is the apparent mass of the immersed sample, and m_3 is the mass of the soaked sample.

2.7. Mercury Porosimetry

The distributions by pore size of the porous mullite ceramics were analyzed using mercury intrusion porosimetry with a US Quantachrome, Pore Master 33. Hg porosimetry allows for the determination of the pore size in the range of 0.1–1000 μm. The pore size determined by Hg porosimetry is related to the range of pressures to be used. The possible detectable pore diameter is inversely proportional to the pressure. Low-pressure mercury

porosimetry determines macropores with pore diameters of 14–200 μm but in a vacuum at 360–950 μm . At first, mercury enters the larger pores, and then, as the total pressure slowly increases, it squeezes into the smaller pores. The pore shape affects the overall pore size distribution graph [32]. In practice, it is assumed that the pores have a cylindrical shape, which is characterized by the modified Jung–Laplace or Washburn Equation (3):

$$\Delta P = \frac{2\gamma \cos \theta}{r_{\text{pore}}} \quad (3)$$

where—pressure change when mercury enters the pore, N/m^2 , Pa;

r_{pore} —corresponding pore radius, μm ;

γ —surface tension of mercury, N/m ;

θ —wetting angle between the solid surface of the material and mercury.

2.8. Thermal Shock Resistance Testing

The thermal shock resistance tests provided a measure of the ability of the ceramic materials to withstand several cycles of thermal stresses when subjected to rapid changes in temperature. Resistance to the rapid change in temperature by the scheme from 20 to 1000 $^{\circ}\text{C}$ with exposure for one hour at this temperature and with the subsequent sharp cooling at 20 $^{\circ}\text{C}$ was determined during 10 such cycles.

2.9. E Modulus Measurement

The value of the E modulus was determined before and after the first, second, third, fifth, and tenth thermal shock tests using an acoustic impulse excitation method with Buzz-O-Sonic 5.0 equipment from BuzzMac International, LLC, Portland, ME, USA. This method is nondestructive and allows for the use of the same samples for all thermal shock cycles. The operating principle of the Buzz-O-Sonic system is based on the excitation of elastic oscillations with an impulse in the material; the created sound is perceived with a microphone connected to a computer. The acoustic system analyzes sound using the fast Fourier transform algorithm. This acoustic signal contains the sample's natural frequencies of vibration, which are proportional to the elastic (Young's) modulus, calculated with Buzz-O-Sonic 5.0 software according to classical beam theory [33].

3. Results and Discussion

3.1. Crystalline Phase Compositions

The X-ray diffraction analysis patterns of the sintered ceramics materials are displayed in Figures 1 and 2. The use of micro- and nano- WO_3 had an influence on the phase composition of the modified porous mullite ceramic. The main crystalline phase of the sintered samples corresponds to mullite (Figure 1). The phase of corundum is slightly observed for the A1 samples (Figure 1a). The mullite ceramic samples with YSZ (A1 and A2) contained monoclinic ZrO_2 (Figure 1a,b). The samples with magnesia-stabilized zirconia (A3 and A4) additionally contained the zircon phase, but the intensity of monoclinic tetragonal ZrO_2 greatly decreased (Figure 1b,c). The formation of zircon could be explained by the reaction of amorphous SiO_2 and ZrO_2 in an equimolar ratio at a temperature of 1200 $^{\circ}\text{C}$ [34,35]. Porous mullite ceramic A1 and A2 samples do not contain the zircon phase due to its dissociation with mullite phase formation after forming a liquid phase in the $\text{Y}_2\text{O}_3\text{--Al}_2\text{O}_3\text{--SiO}_2$ system at 1550 $^{\circ}\text{C}$ [36,37]. The addition of nano- WO_3 did not affect zircon formation in the cases of the A1 and A2 samples. The use of nano- WO_3 in compositions with magnesia-stabilized zirconia and microsize WO_3 in 1:1 and 1:2 ratios, respectively, caused the formation of a zircon phase due to preventing zircon dissipation in the $\text{MgO--Al}_2\text{O}_3\text{--SiO}_2$ system in possibly emerging liquid at 1450–1550 $^{\circ}\text{C}$, as in the case of the $\text{Y}_2\text{O}_3\text{--Al}_2\text{O}_3\text{--SiO}_2$ system.

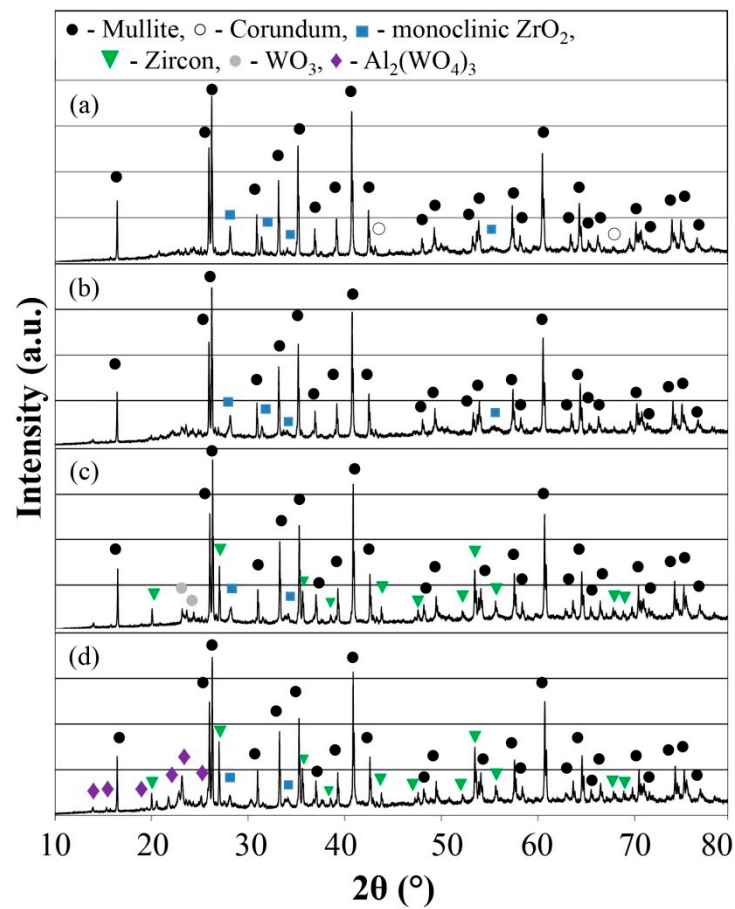


Figure 1. XRD of the investigated porous ceramic samples: (a) Sample A1; (b) Sample A2; (c) Sample A3; (d) Sample A4.

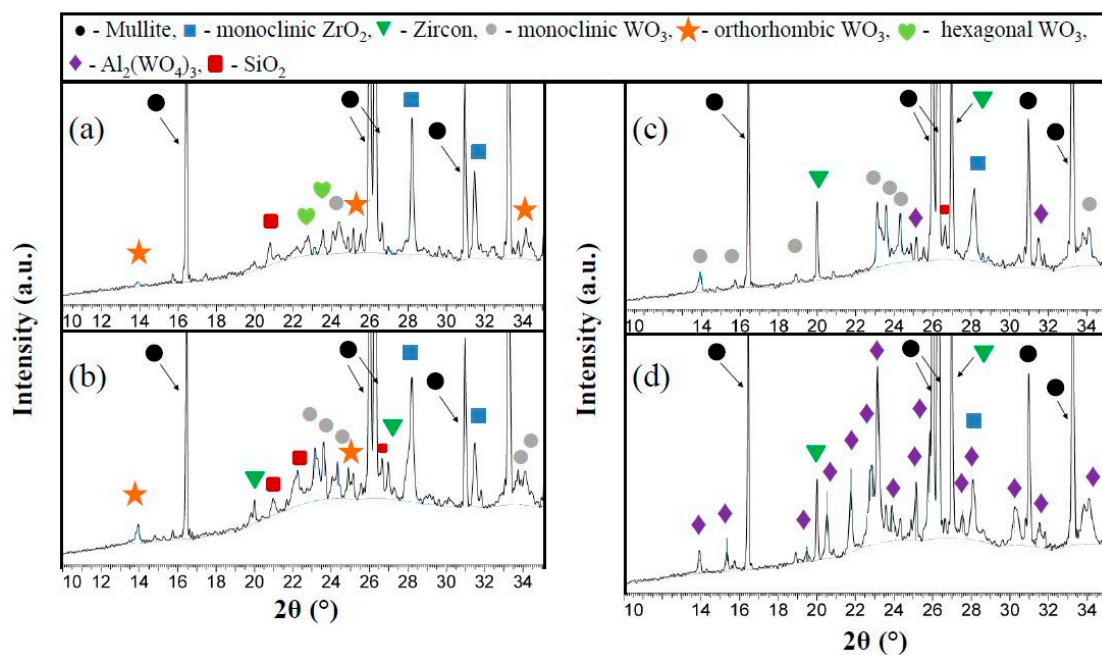


Figure 2. X-ray diffraction data from 0° 2θ to 35° 2θ of the sintered porous ceramic materials: (a) A1 sample; (b) A2 sample; (c) A3 sample; (d) A4 sample.

Figure 2 displays the X-ray diffraction patterns from $10^\circ 2\theta$ to $35^\circ 2\theta$ of the prepared ceramics. It can be seen that, as expected, all samples have crystalline as well as amorphous phases. The A1 ceramic samples from the composition of the YSZ and WO_3 mixture in a 1:1 ratio and nano- WO_3 have additional phases as orthorhombic and hexagonal WO_3 (Figure 2a) [38–40]. The A2 samples have orthorhombic and monoclinic WO_3 (Figure 2b). Figure 2c shows that in the case of the A3 samples, the diffraction peaks correspond to the planes of (002), (200), (020), (120), (022), and (202), proving the monoclinic phase of tungsten trioxide. It is also possible that a slight presence of the aluminum tungstate phase is presented in these samples, because some intensity peaks of $\text{Al}_2(\text{WO}_4)_3$ and WO_3 overlap each other. The XRD patterns of the A4 sample (Figure 2d) show the presence of $\text{Al}_2(\text{WO}_4)_3$. The separate diffraction peaks in the $2\theta^\circ$ range from 14° to 26° , at 30.5° , 31.5° , 34° , and 35° correspond to the aluminum tungstate phase [41,42].

3.2. Macrostructure and Microstructure

Figure 3 shows the macrostructure and microstructure of the A1 samples. The A1 samples consist of densely packed mullite crystals. In turn, between the mullite crystals, there is a glassy phase containing WO_3 that confirms the EDS point analysis in Table 1. Such a glassy phase is uniformly distributed at the structure and displays as lighter parts on the SEM micrographs in Figure 3a,b.

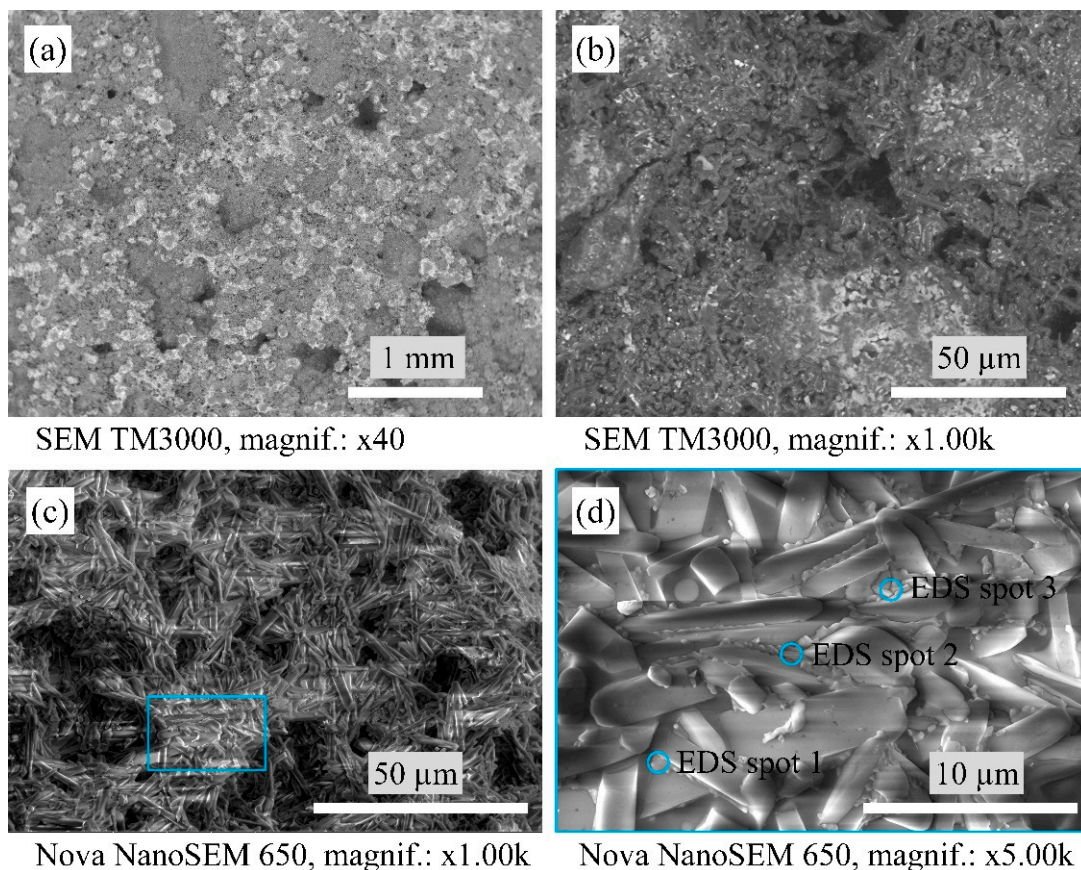


Figure 3. Micrographs of the sintered A1 samples' microstructure with SEM.

The structure of the porous mullite ceramic samples with a mixture of YSZ and tungsten trioxide in a 1:2 ratio and nano- WO_3 additive (A2 sample, Figure 4) is more loose than the structure of the A1 sample. The glassy phase containing different WO_3 is also shown as white particles and areas on the SEM micrographs.

Table 1. Elemental composition with EDX point analysis of the A1 sample.

Elements	EDS Spot 1		EDS Spot 2		EDS Spot 3	
	wt%	Atomic%	wt%	Atomic%	wt%	Atomic%
O K	42.4	65.9	38.5	70.4	47.3	70.7
AlK	23.5	21.7	18.8	20.4	20.6	18.3
SiK	9.5	8.4	3.9	1.3	8.4	7.2
W M	19.7	2.7	34.0	5.4	19.4	2.5
Y L	3.3	0.9	3.3	1.1	2.7	0.7
ZrL	1.6	0.4	1.5	1.4	1.6	0.6

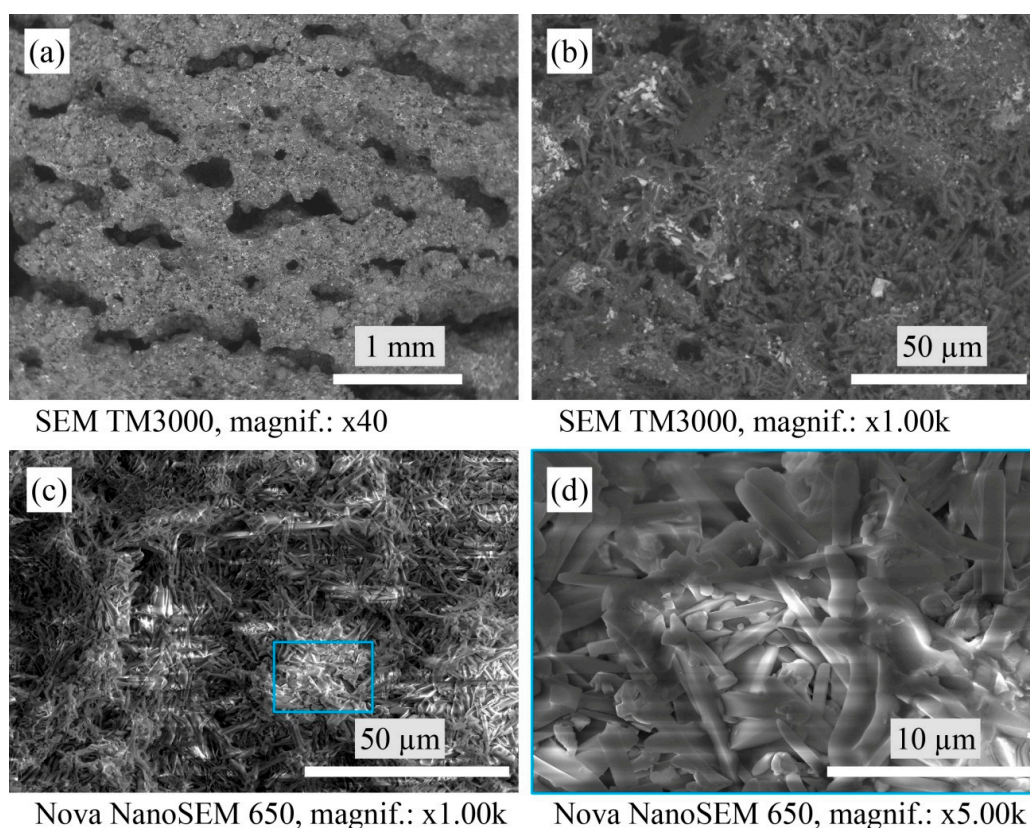
**Figure 4.** Micrographs of the sintered A2 samples' microstructure with SEM.

Figure 5 shows the evenly distributed agglomerates of monoclinic WO_3 in the structure, seen as white areas on the SEM of the A3 sample. The faceted zircon crystals can be visible at higher SEM magnification, as shown in Figure 5d.

SEM and mapping EDS analysis were performed for the porous mullite ceramic A4 samples, the raw material compositions of which contained a mixture of magnesia-stabilized zirconia and tungsten trioxide in a 1:2 ratio and nano- WO_3 additive (Figures 6 and 7). Figure 6a,b show the white phase that according to XRD analysis corresponds to aluminum tungstate. Its presence is clearly observed in many areas, as determined by EDS analysis (Figure 7).

The SEM and mapping EDS analysis in Figure 7 allow for the designation of two types of mullite crystals that differ in size and aspect ratio. Two areas define the mullite crystals after the EDX results: the A and C phases (red and blue colors, respectively). The A4 samples' structure is formed as thick long acicular crystals as well as thin elongated needle-shaped mullite crystals. The C phase corresponds to larger mullite crystals, but the A phase corresponds to thinner mullite crystals after EDX mapping results (Table 2). The width to length ratio of the thick mullite crystals is in the 15–22:1 interval. The needle-like thin mullite crystals are showing an aspect ratio of approximately 11:1 (with a length of 0.5–1.5 μm and a width of 0.1–0.2 μm).

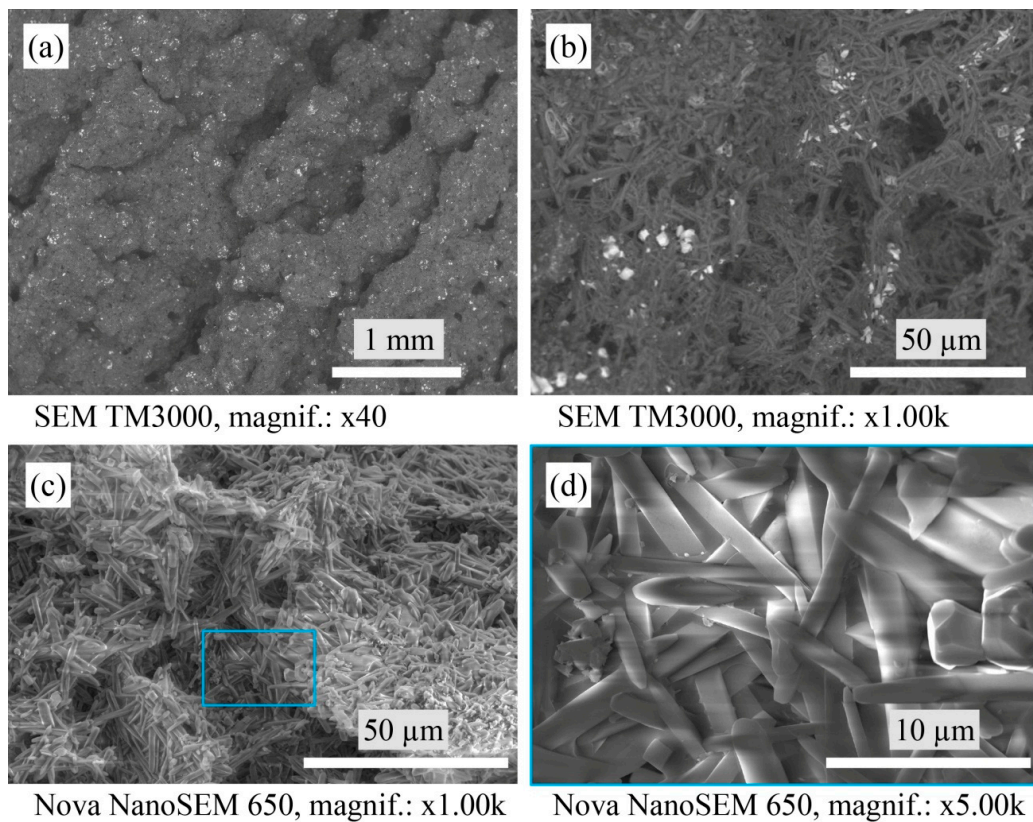


Figure 5. Micrographs of the sintered A3 samples' microstructure with SEM.

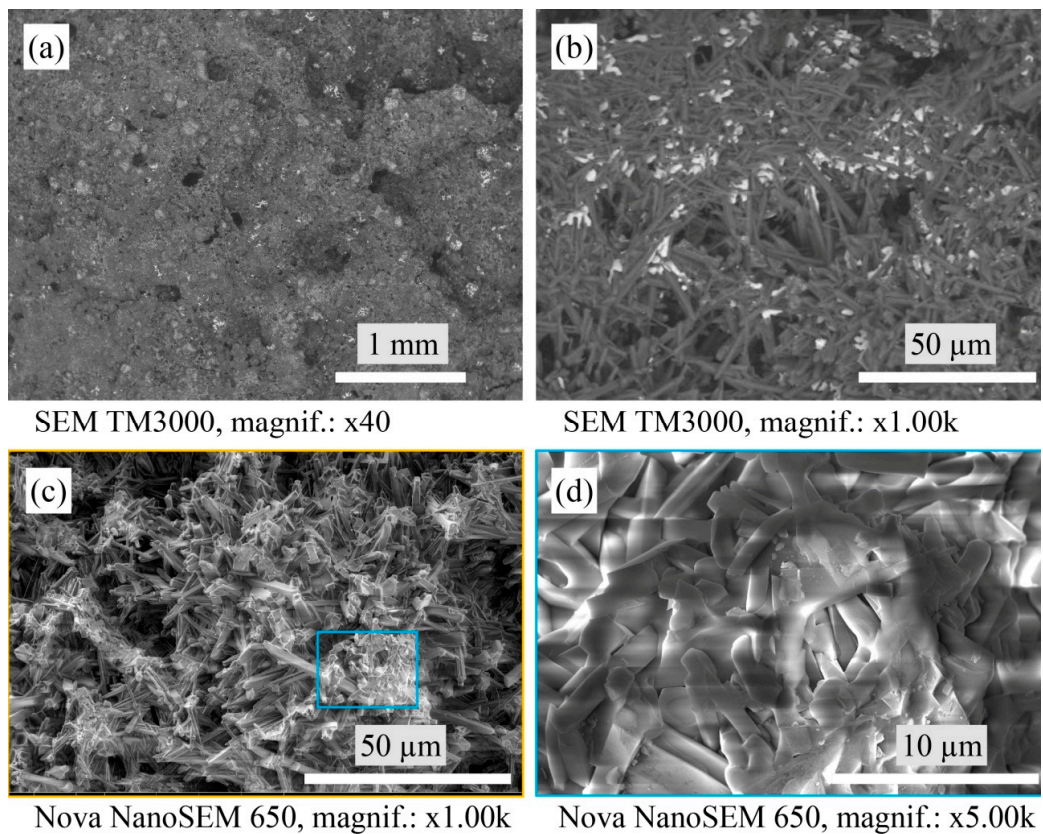


Figure 6. Micrographs of the sintered A4 samples' microstructure with SEM.

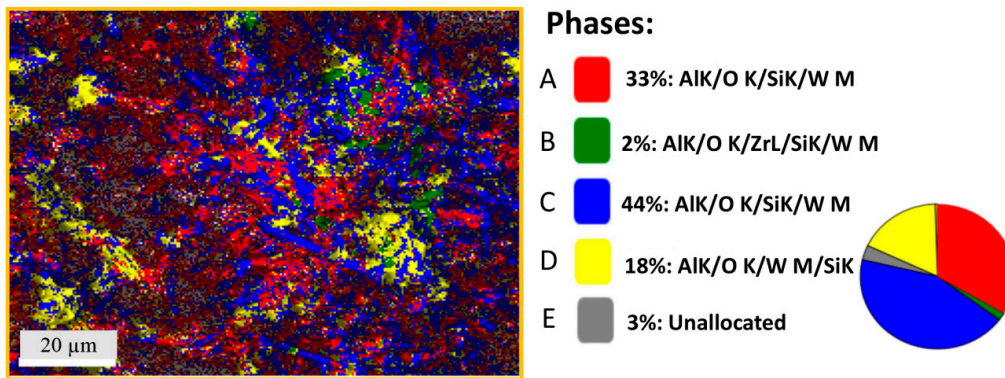


Figure 7. Energy dispersive spectroscopy mapping analysis of the sintered A4 sample. The EDX micrograph corresponds to the SEM micrograph in Figure 6c.

Table 2. Elemental composition with EDX analysis of the A4 sample.

Elements	Phase A		Phase B		Phase C		Phase D	
	wt%	Atomic%	wt%	Atomic%	wt%	Atomic%	wt%	Atomic%
O K	33.6	46.9	43.3	67.9	48.5	62.8	44.0	61.9
AlK	49.0	40.5	13.0	12.2	34.8	26.7	24.6	20.4
SiK	15.6	12.4	13.7	12.2	13.6	10.0	20.3	16.2
W M	1.8	0.2	3.8	0.5	2.6	0.3	10.3	1.3
ZrL	0	0	26.2	7.2	0.5	0.2	0.8	0.2

Figure 7 shows that phase B (green color) takes a lower percentage place among the other phases. Phase B corresponds to the phase of zircon according to the elemental composition by EDX analysis of the A4 sample. The EDX mapping and Table 2 show that the D phase (yellow color) has a high weight percentage of such chemical elements as O, Al, Si, and W but a low weight percentage of zirconium, which can confirm the aluminum tungstate crystalline phase, as well as the aluminum tungstate glassy phase in these areas. In turn, the elemental composition of the A4 sample (Figure 8) shows that the W element is evenly distributed in the sample structure, in contrast to the distribution of the Zr element. By comparing the XRD results and EDX of the A4 sample, it can be concluded that the aluminum tungstate phase is evenly distributed in the structure of these samples.

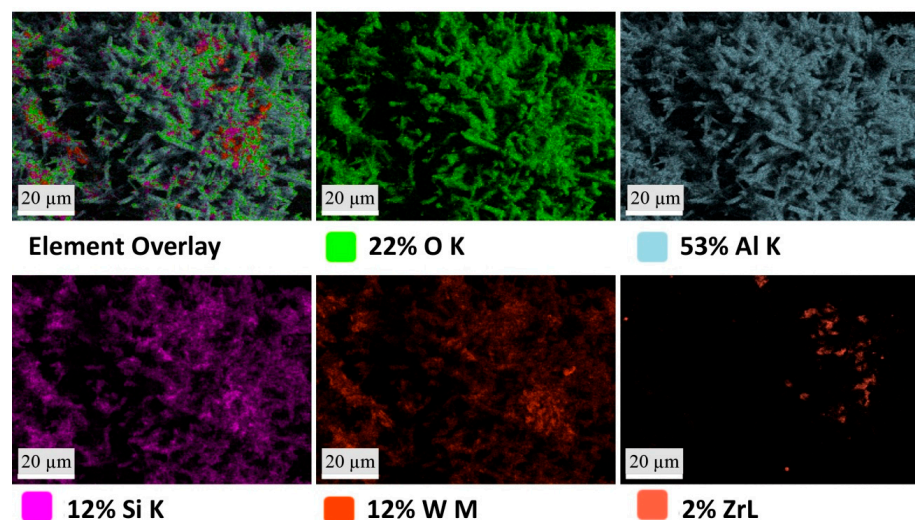


Figure 8. SEM-EDX micrographs of the element distribution in the structure of the A4 samples.

The SEM results reveal that the morphologies of the microstructures of the A1 and A3 samples present significant similarities due to the amorphous phase between the mullite crystals. In turn, the amorphous phase is not observed between the mullite crystals in the A2 and A4 samples.

3.3. Bulk Density and Change in Samples' Dimensions

The bulk density and percent change in the samples' dimensions after sintering or sample shrinkage are shown in Figure 9. The A1 sample that was modified with a mixture of yttria-stabilized zirconia and tungsten trioxide in a 1:1 ratio plus nano-WO₃ has a higher bulk density of approximately 1.60 ± 0.05 g/cm³. The other samples, A2, A3, and A4, have a bulk density of approximately 1.25 ± 0.05 g/cm³. The A1 sample has a more densely packed structure due to the presence of an amorphous phase around the mullite crystals. The A1 and A2 samples from the compositions with YSZ and WO₃, respectively, in a 1:1 ratio and 1:2 plus nano-WO₃ have higher shrinkage than the A3 and A4 samples from the compositions with MSZ and WO₃, respectively, in a 1:1 ratio and 1:2 plus nano-WO₃. The usage of YSZ increased the shrinkage of the samples by $\approx 10\%$ in comparison with the samples with MSZ due to the formation of a liquid phase in the Y₂O₃-Al₂O₃-SiO₂ system.

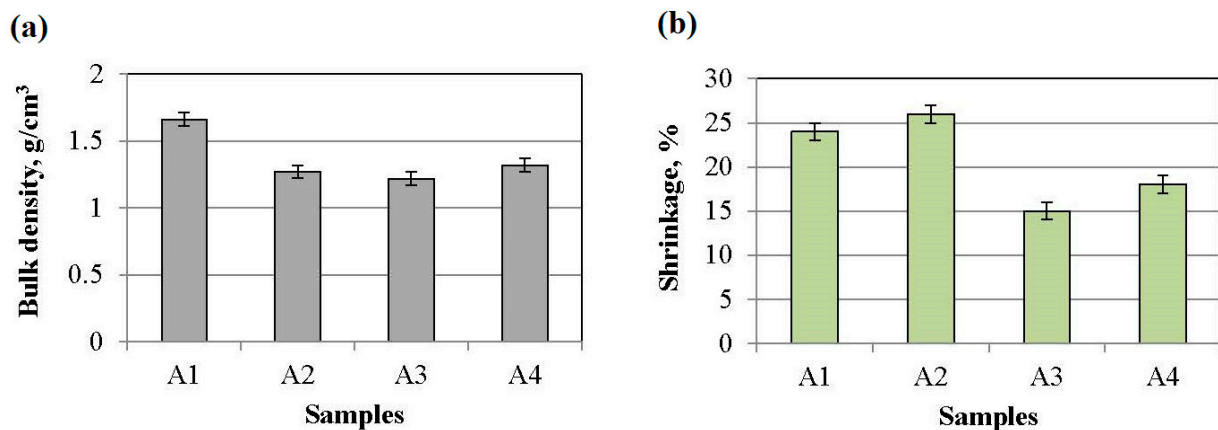


Figure 9. Sample characterizations: (a) bulk density and (b) shrinkage.

3.4. Apparent Porosity, Water Uptake, and Pore Sizes

The apparent porosity of the sintered samples is shown in Figure 10. The A1 sample with the higher bulk density has a smaller apparent porosity of approximately $40 \pm 2\%$ and water uptake of approximately $25 \pm 1\%$. This is due to the YSZ (8 mol% Y₂O₃), which influenced the formation of a liquid phase that decreased the porosity. Doubling of WO₃ prevents liquid formation in the system of Y₂O₃-WO₃, as well as in samples with magnesia-stabilized zirconia. The samples of A2, A3, and A4 have porosity higher than $63 \pm 1\%$ and water uptake of approximately $40 \pm 1\%$.

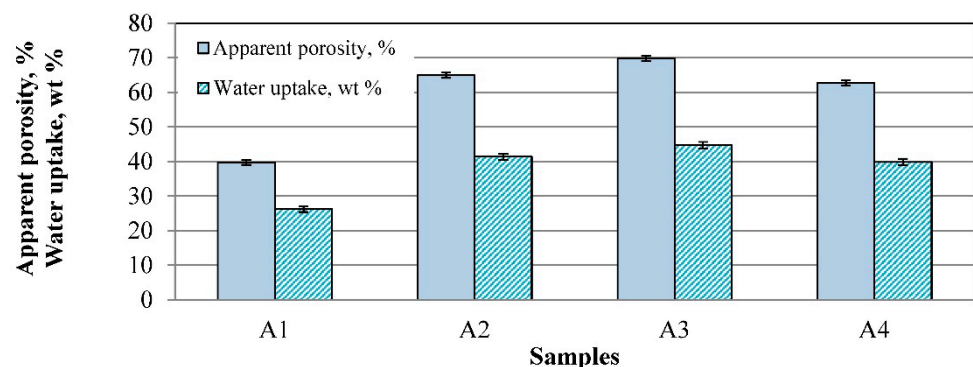


Figure 10. Apparent porosity of the investigated samples.

Figure 11 shows the pore size distribution after mercury intrusion porosimetry. One or two ranges of pore size distributions are observed in the investigated ceramics. In comparison with the other samples, the A1 sample has one narrow range of pore size distributions of approximately 2–15 μm , with pronouncing of pores of 8 μm size. It can be assumed that due to the composition, the formed amorphous phase partially filled pores larger than 15 microns, and thus only pores in a smaller size range remained. The other samples, A2, A3, and A4, have two ranges of pore size distributions. These ranges are from 2 μm to 15 μm and from 15 μm to 1000 μm . The most pronounced pore sizes in these samples are approximately 5–7 μm and 100–200 μm .

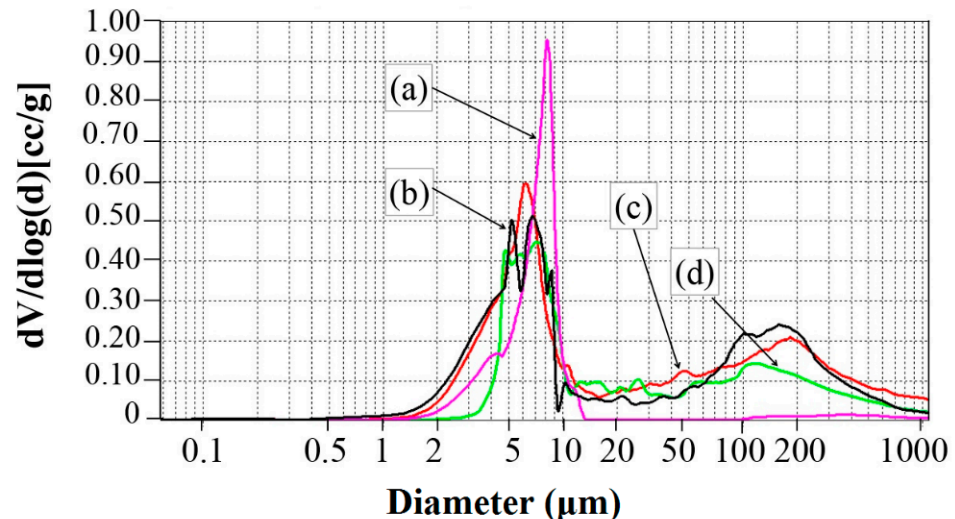


Figure 11. Distributions of the samples' pore sizes: (a) sample A1; (b) sample A2; (c) sample A3; (d) sample A4.

3.5. Resistance to Thermal Shock

The relative changes in the E modulus of the sintered samples after the thermal shock tests (10 cycles) are shown in Figure 12. All samples have high stability from the first to the fifth cycle of the rapid temperature change by the scheme from 20 $^{\circ}\text{C}$ to 1000 $^{\circ}\text{C}$ and back to 20 $^{\circ}\text{C}$ with holding for one hour at a temperature of 1000 $^{\circ}\text{C}$. In this case, the elastic modulus losses do not exceed 5%, which is a high rate. The thermal shock resistance for each sample depends on individual factors. The A1 and A4 samples have a small relative change in the E modulus after the testing of 10 thermal shock cycles, which is less than 5%. In the case of the A1 sample, the positive influence lies in the presence of evenly distributed pores, with a range of pore size distributions from 2 μm to 15 μm and a phase composition of mullite and monoclinic ZrO_2 , which prevents the formation and growth of cracks.

The A2, A3, and A4 samples have two distinct arrays of pore sizes of relatively small (2–15 μm) and larger (15–1000 μm) size. The values of the E modulus of the A2 and A3 samples decreased significantly after the 10th cycle and, respectively, are 20% and 15% due to the preservation of WO_3 with high LTEC and critical crack growth in the process of the 10th cycle. The A4 samples can better resist the sudden change in temperature due to the crystallinity structure and phase compositions from mullite, zircon, and aluminum tungstate. Mullite and zircon have low thermal expansion, respectively, from 4.0 to $5.9 \cdot 10^{-6} \cdot ^{\circ}\text{K}^{-1}$ [43] and $4.1 \cdot 10^{-6} \cdot ^{\circ}\text{K}^{-1}$ [44] between temperatures of 30 $^{\circ}\text{C}$ and 1000 $^{\circ}\text{C}$, and aluminum tungstate has a negative thermal expansion of $-1.5 \cdot 10^{-6} \cdot ^{\circ}\text{K}^{-1}$ in the temperature diapason of 25–850 $^{\circ}\text{C}$ [45], which prevents thermal stress formation at the time of the thermal shock.

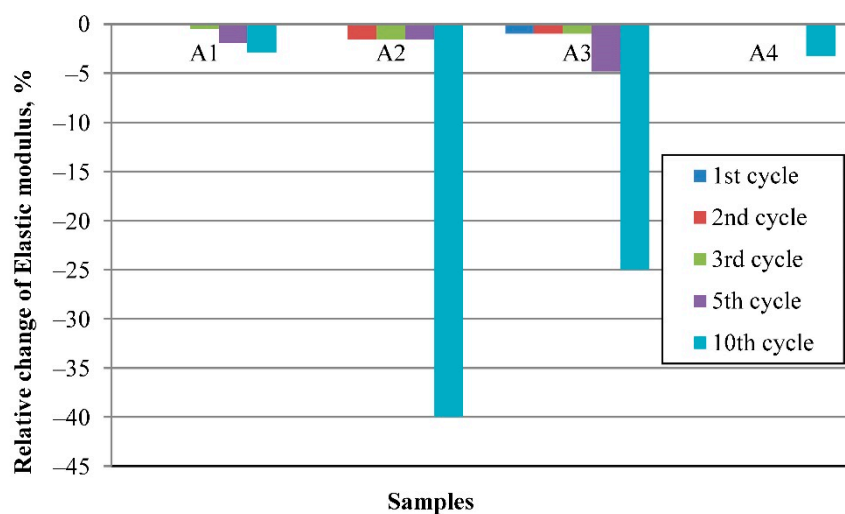


Figure 12. E modulus relative change after thermal shock testing of the samples.

4. Conclusions

The influence of porous mullite ceramic modification with differently stabilized micro-sized ZrO_2 and WO_3 , as well as with nanosized WO_3 , on the different properties of highly porous mullite ceramic materials was investigated. The use of kaolin as a binder, as well as the mixing of the initial raw materials with a technical mixer and raw material suspension slip casting, make it possible to obtain a uniform distribution of raw materials, including nanosized ones. In combination with these oxide compositions, the addition of a small percentage of nano- WO_3 had an effect on the formation of aluminum tungstate with negative LTEC and zircon with low LTEC. The use of nano- WO_3 prevented the dissociation of zircon in the ceramic samples with magnesia-stabilized zirconia and increased the intensity of the aluminum tungstate phase in the investigated materials with MSZ and WO_3 in a 1:2 ratio, which made it possible to obtain mullite ceramics with increased resistance to thermal shock.

Author Contributions: Conceptualization, L.M.-G. and V.G.; methodology, L.M.-G., R.S. and V.S.; validation, L.M.-G., S.I., M.R. and I.J.; formal analysis, L.M.-G., S.I., T.V.E. and A.P.; investigation, L.M.-G.; resources, L.G. and I.J.; data curation, L.M.-G. and M.R.; writing—original draft preparation, L.M.-G.; writing—review and editing, L.M.-G.; visualization, L.M.-G. and V.G.; supervision, R.S. and V.S. All authors have read and agreed to the published version of the manuscript.

Funding: This research was funded by the European Regional Development Fund within the Activity 1.1.1.2 “Post-doctoral Research Aid” of the Specific Aid Objective 1.1.1 “To increase the research and innovative capacity of scientific institutions of Latvia and the ability to attract external financing, investing in human resources and infrastructure” of the Operational Programme “Growth and Employment” (No.1.1.1.2/VIAA/1/16/121).

Institutional Review Board Statement: Not applicable.

Informed Consent Statement: Not applicable.

Data Availability Statement: The data presented in this study are available on request from the corresponding author.

Conflicts of Interest: The authors declare no conflict of interest.

References

1. Wang, F.; Hao, S.; Dong, B.; Ke, N.; Khan, N.Z.; Hao, L.; Yin, L.; Xu, X.; Agathopoulos, S. Porous-foam mullite-bonded SiC-ceramic membranes for high-efficiency high-temperature particulate matter capture. *J. Alloys Compd.* **2022**, *893*, 162231. [[CrossRef](#)]
2. Aryal, S.; Rulis, P.; Ching, W.-Y. Mechanical properties and electronic structure of mullite phases using first-principles modeling. *J. Eur. Ceram. Soc.* **2012**, *95*, 2075–2088. [[CrossRef](#)]

3. Hammel, E.C.; Ighodaro, O.L.-R.; Okoli, O.I. Processing and properties of advanced porous ceramics: An application based review. *Ceram. Int.* **2014**, *140*, 15351–15370. [[CrossRef](#)]
4. Hemra, K.; Aungkavattana, P. Effect of zirconia content on mechanical and thermal properties of mullite–zirconia composite. *Adv. Appl. Ceram.* **2014**, *113*, 323–327. [[CrossRef](#)]
5. Hsiung, C.-H.H.; Pyzik, A.J.; Gulsoy, E.B.; Carlo, F.; Xiao, X.; Faber, K.T. Impact of doping on the mechanical properties of acicular mullite. *J. Eur. Ceram. Soc.* **2013**, *33*, 1955–1965. [[CrossRef](#)]
6. Ouali, A.; Heraiz, M.; Sahnoune, F.; Belhouchet, H.; Fatmi, M.; Saheb, N. Effect of MgO addition on the mechanical and thermal properties of mullite synthesised through reaction sintering of Al₂O₃ and Algerian kaolin. *Am. J. Mod. Phys.* **2013**, *5*, 270–275. [[CrossRef](#)]
7. Salomão, R.; Oliveira, K.; Fernandes, L.; Tiba, P.; Prado, U. Porous refractory ceramics for high-temperature thermal insulation Part 1: The Science Behind Energy Saving. *Interceram Int. Ceram. Rev.* **2021**, *70*, 38–45. [[CrossRef](#)]
8. Zhang, L.; Zhou, D.; Chen, Y.; Liang, B.; Zhou, J. Preparation of high open porosity ceramic foams via direct foaming molded and dried at room temperature. *J. Eur. Ceram. Soc.* **2014**, *34*, 2443–2452. [[CrossRef](#)]
9. Pirzada, T.J.; Liu, D.; Ell, J.; Barnard, H.; Šulak, I.; Galano, M.; Marrow, T.J.; Ritchie, R.O. In situ observation of the deformation and fracture of an alumina-alumina ceramic-matrix composite at elevated temperature using X-ray computed tomography. *J. Eur. Ceram. Soc.* **2021**, *41*, 4217–4230. [[CrossRef](#)]
10. Zhua, Z.; Wei, Z.; Shen, J.; Zhuc, L.; Xu, L.; Zhang, Y.; Wang, S.; Liu, T. Fabrication and catalytic growth mechanism of mullite ceramic whiskers using molybdenum oxide as catalyst. *Ceram. Int.* **2017**, *43*, 2871–2875. [[CrossRef](#)]
11. Zhao, H.; Li, X.; Ji, H.; Yu, H.; Yu, B.; Qi, T. Constructing secondary-pore structure by in-situ synthesized mullite whiskers to prepare whiskers aerogels with ultralow thermal conductivity. *J. Eur. Ceram. Soc.* **2019**, *39*, 1344–1351. [[CrossRef](#)]
12. Yang, P.; Liu, S.; Mao, Z.; Wang, D. Preparation and properties of hierarchical structural alumina/mullite composites. *J. Eur. Ceram. Soc.* **2023**, *43*, 468–477. [[CrossRef](#)]
13. Qin, Z.; Xu, X.; Xu, T.; Cao, Y.; Wu, J.; Yan, L.; Hou, F.; Liu, J.; Guo, A. High-strength thermal insulating porous mullite fiber-based ceramics. *J. Eur. Ceram. Soc.* **2022**, *42*, 7209–7218. [[CrossRef](#)]
14. Yang, Z.; Yang, F.; Zhao, S.; Li, K.; Chen, J.; Fei, Z.; Chen, G. In-situ growth of mullite whiskers and their effect on the microstructure and properties of porous mullite ceramics with an open/closed pore structure. *J. Eur. Ceram. Soc.* **2021**, *41*, 299–308. [[CrossRef](#)]
15. Qiao, M.; Li, X.; Chen, P.; Zhu, Y.; Zhu, B. Pore evolution and slag resistance of corundum castables with nano zirconia addition. *Ceram. Int.* **2021**, *47*, 6947–6954. [[CrossRef](#)]
16. Dudczig, S.; Veres, D.; Aneziris, C.G.; Skiera, E.; Steinbrech, R.W. Nano- and micrometre additions of SiO₂, ZrO₂ and TiO₂ in fine grained alumina refractory ceramics for improved thermal shock performance. *Ceram. Int.* **2012**, *38*, 2011–2019. [[CrossRef](#)]
17. Badiie, S.H.; Otraj, S. The effect of nano-titania addition on the properties of high-alumina low-cement self-flowing refractory castables. *Ceram. Silik.* **2011**, *55*, 319–325.
18. Qian, L.; Yang, L.; Li, G.; Jiang, W.; Fan, Z. Effect of nano-TiO₂ on properties of 3 mol% yttria-stabilized zirconia ceramic via layered extrusion forming. *J. Eur. Ceram. Soc.* **2020**, *40*, 4539–4546. [[CrossRef](#)]
19. Khaskhoussi, A.; Calabrese, L.; Bouaziz, J.; Proverbio, E. Effect of TiO₂ addition on microstructure of zirconia/alumina sintered ceramics. *Ceram. Int.* **2017**, *43*, 10392–10402. [[CrossRef](#)]
20. Esmaili, M.; Nilforoushan, M.R.; Tayebi, M.; Aghaie, E. Effect of micro/nano TiO₂ addition on the densification behavior and mechanical properties of multifunctional resistant porcelains. *Ceram. Int.* **2021**, *47*, 17435–17444. [[CrossRef](#)]
21. Ghasemi-Kahrizangi, S.; Sedeh, M.B.; Dehsheikh, H.G.; Shahraki, A.; Farooghi, M. Densification and properties of ZrO₂ nanoparticles added magnesia–dolomite refractories. *Ceram. Int.* **2016**, *42*, 15658–15663. [[CrossRef](#)]
22. Gogtas, C.; Lopez, H.F.; Sobolev, K. Effect of nano-YSZ and nano-ZrO₂ additions on the strength and toughness behavior of self-flowing alumina castables. *Ceram. Int.* **2016**, *42*, 1847–1855. [[CrossRef](#)]
23. Wang, F.; Dong, B.; Wang, J.; Ke, N.; Tan, C.; Huang, A.; Wu, Y.; Hao, L.; Yin, L.; Xu, X.; et al. Self-supported porous heterostructure WC/WO_{3-x} ceramic electrode for hydrogen evolution reaction in acidic and alkaline media. *J. Adv. Ceram.* **2022**, *11*, 1208–1221. [[CrossRef](#)]
24. Dutta, V.; Sharma, S.; Raizada, P.; Thakur, V.K.; Khan, A.A.P.; Saini, V.; Asiri, A.M.; Singh, P. An overview on WO₃ based photocatalyst for environmental remediation. *J. Environ. Chem. Eng.* **2021**, *9*, 105018. [[CrossRef](#)]
25. Anandaraj, C.; Bharath Sabarish, V.C.; Durairajan, A.; Graca, M.P.F.; Valente, M.A.; Gajendiran, J.; Raj, S.G.; Kumar, G.R. Influence of tungsten trioxide (WO₃) on the topographical, structural, optical absorption and electrochemical characteristics of BFO-MWCNT and BFO-Graphene nanocomposite ceramics. *Chem. Phys.* **2022**, *563*, 111699. [[CrossRef](#)]
26. Ji, C.; Wang, J.; Bai, X.; Hao, M.; Chen, G.; He, J.; Fan, T.; Zhang, Z.; Chen, C.; Fu, C. Effects of MnO₂ and WO₃ co-doping and sintering temperature on microstructure, microwave dielectric properties of Ba₂Ti₉O₂₀ microwave ceramics. *Ceram. Int.* **2022**, *48*, 10713–10720. [[CrossRef](#)]
27. Vadivel, S.; Saravanakumar, B.; Kumaravel, M.; Maruthamani, D.; Balasubramanian, N.; Manikand, A.; Ramadoss, G.; Paul, B.; Hariganesh, S. Facile solvothermal synthesis of BiOI microsquares as a novel electrode material for supercapacitor applications. *Mater. Lett.* **2018**, *210*, 109–112. [[CrossRef](#)]
28. Paul, B.; Manwar, N.; Bhanja, P.; Sellaiyan, S.; Sharma, S.K.; Khatun, R.; Jain, S.; Bal, R. Morphology controlled synthesis of 2D heterostructure Ag/WO₃ nanocomposites for enhanced photoelectrochemical CO₂ reduction performance. *J. CO₂ Util.* **2020**, *41*, 101284. [[CrossRef](#)]

29. Paul, B.; Sharma, S.; Purkayasthab, D.D.; Dharb, S.S.; Bala, R. Facile synthesis of size-controlled Ag supported on WO₃ nanorods and their application as novel and active catalyst in oxidant-free dehydrogenation of benzyl alcohols. *Catal. Commun.* **2019**, *132*, 105804. [[CrossRef](#)]
30. Mahnicka-Goremikina, L.; Svinka, R.; Svinka, V. Influence of ZrO₂ and WO₃ doping additives on the thermal properties of porous mullite ceramics. *Ceram. Int.* **2018**, *44*, 16873–16879. [[CrossRef](#)]
31. DIN EN 623-2:1993; Advanced Technical Ceramics; MONOLITHIC ceramics; General and Textural Properties; Determination of Density and Porosity. European standards, 1993.
32. Salmas, C.; Androustopoulos, G. Mercury Porosimetry: Contact Angle Hysteresis of Materials with Controlled Pore Structure. *J. Coll. Interf. Sci.* **2001**, *239*, 178–189. [[CrossRef](#)]
33. Kutz, M. *Handbook of Materials Selection*; John Wiley & Sons: New York, NY, USA, 2002; 1497p.
34. Itoh, T. Formation of polycrystalline zircon (ZrSiO₄) from amorphous silica and amorphous zirconia. *J. Cryst. Growth* **1992**, *125*, 223–228. [[CrossRef](#)]
35. Mori, T.; Yamamura, H.; Kobayashi, H.; Mitamura, T. Formation mechanism of ZrSiO₄ powders. *J. Mater. Sci.* **1993**, *28*, 4970–4973. [[CrossRef](#)]
36. Awaad, M.; Zawrah, M.F.; Khalil, N.M. In situ formation of zirconia–alumina–spinel–mullite ceramic composites. *Ceram. Int.* **2008**, *34*, 429–434. [[CrossRef](#)]
37. Nozahic, F.; Carabat, A.L.; Mao, W.; Monceau, D.; Estournes, C.; Kwakernaak, C.; Zwaag, S.; Sloof, W.G. Kinetics of zircon formation in yttria partially stabilized zirconia as a result of oxidation of embedded molybdenum disilicide. *Acta Mater.* **2019**, *174*, 206–2016. [[CrossRef](#)]
38. Wang, L.; Hu, H.; Xu, J.; Zhu, S.; Ding, A.; Deng, C. WO₃ nanocubes: Hydrothermal synthesis, growth mechanism, and photocatalytic performance. *J. Mater. Res.* **2019**, *34*, 2955–2963. [[CrossRef](#)]
39. Ponnusamy, R.; Gangan, A.; Chakraborty, B.; Sekhar Rout, C. Tuning the pure monoclinic phase of WO₃ and WO₃-Ag nanostructures for non-enzymatic glucose sensing application with theoretical insight from electronic structure simulations. *J. Appl. Phys.* **2018**, *123*, 024701. [[CrossRef](#)]
40. Chacon, C.; Rodriguez-Perez, M.; Oskam, G.; Rodriguez-Gattorno, G. Synthesis and characterization of WO₃ polymorphs: Monoclinic, orthorhombic and hexagonal structures. *J. Mater. Sci. Mater. Electron.* **2015**, *26*, 5526–5531. [[CrossRef](#)]
41. Koseva, I.I.; Nikolov, V.S. Preparation of aluminum tungstate Al₂(WO₄)₃ using sol-gel modified Pechini method. *Bul. Chem. Com.* **2010**, *42*, 300–304.
42. Batista, F.M.C.; La Porta, F.A.; Gracia, L.; Cerdeiras, E.; Mestres, L.; Siu Li, M.; Batista, N.C.; Andrés, J.; Longo, E.; Cavalcante, L.S. A joint experimental and theoretical study on the electronic structure and photoluminescence properties of Al₂(WO₄)₃ powders. *J. Mol. Struc.* **2015**, *1081*, 381–388. [[CrossRef](#)]
43. Foo, C.T.; Salleh, M.A.M.; Ying, K.K.; Matori, K.A. Mineralogy and thermal expansion study of mullite-based ceramics synthesized from coal fly ash and aluminum dross industrial wastes. *Ceram. Int.* **2019**, *45*, 7488–7494. [[CrossRef](#)]
44. Rendtorff, N.M.; Garrido, L.B.; Aglietti, E.F. Thermal shock resistance and fatigue of Zircon–Mullite composite materials. *Ceram. Int.* **2011**, *37*, 1427–1434. [[CrossRef](#)]
45. Achary, S.N.; Mukherjee, G.D.; Tyagi, A.K.; Vaidya, S.N. Preparation, thermal expansion, high pressure and high temperature behaviour of Al₂(WO₄)₃. *J. Mater. Sci.* **2002**, *37*, 2501–2509. [[CrossRef](#)]

Disclaimer/Publisher’s Note: The statements, opinions and data contained in all publications are solely those of the individual author(s) and contributor(s) and not of MDPI and/or the editor(s). MDPI and/or the editor(s) disclaim responsibility for any injury to people or property resulting from any ideas, methods, instructions or products referred to in the content.